Soft Matter

PAPER

View Article Online
View Journal | View Issue

Cite this: *Soft Matter*, 2025, **21**, 9112

Confinement effects in microphase separated block copolymer electrolytes – conductivity and crystallinity

Michael Patrick Blatt,[ab] Stephanie Posedel,[ab] Kyoungmin Kim[ab] and Daniel T. Hallinan Jr *[ab]

A series of strongly microphase separated block copolymers of polystyrene (PS) and poly(ethylene oxide) (PEO) were studied with morphologies of spheres, cylinders, and lamellae. Each morphology comprised two samples, one with glassy PS as the majority component and one with semicrystalline PEO as the majority block. Complementary block copolymer (BCP) electrolytes were formed by mixing each BCP with lithium bis(trifluoromethanesulfonylimide) (LiTFSI) salt. The thermal and ion transport properties of these neat and electrolyte BCPs did not exhibit clear trends with respect to either PEO volume fraction or effective medium theory predictions, which prompted an examination of the confinement of the PEO conductive phase. The domain spacing of each morphology was measured with X-ray scattering, and a confinement length was defined as the characteristic PEO domain size in PEO-minority BCPs or the minimum distance between two non-conductive PS microdomains in PEO-majority BCPs. Confinement was found to impede crystallization in an exponentially decaying fashion with an exponential constant of 15 nm, which is similar to PEO crystal lamella size. The dependence of conductivity on confinement was found to be more nuanced. Confinement was detrimental to ionic conductivity in lamellar morphologies, approaching the effective-medium prediction with increasing confinement length (*i.e.* less confined). Conversely, in morphologies with curvature, conductivity was enhanced, increasing strongly with decreasing confinement length. This remarkable result could be leveraged to design more conductive polymer electrolytes for solid state batteries.

Received 27th May 2025,
Accepted 2nd November 2025

DOI: 10.1039/d5sm00554j

rsc.li/soft-matter-journal

Introduction

Batteries enable the integration of intermittent clean energy production modalities, such as wind and solar, with applications such as electric vehicles and domestic power grids.[1] The Li-ion battery has long been the epitome of practical energy storage due to its high power output per unit mass and cycle stability compared to preceding and contemporary technologies.[2] New battery chemistries offer a potential means for disruptive and significant improvement over the Li-ion battery benchmark. One potential innovation is the lithium metal battery (LMB) as, from a purely specific capacity perspective, the lithium metal anode is a decisive improvement over Li-ion anodes such as graphite. Due to the lack of an ion housing substrate, like the carbon atoms used in the graphite electrode, the lithium metal anode has up to an order of magnitude higher specific capacity (3860 mAh g^{-1}) as compared to anodes that rely on intercalation.[3]

Despite this, the adoption of the lithium metal anode has been hampered by its reactivity with conventional liquid electrolytes.[4] Polymer electrolytes have long been studied as a potential means to enable the use of the lithium metal anode due to their much greater chemical compatibility with lithium metal.[4] Despite this, the low room temperature ionic conductivity (κ) of polymer electrolytes relative to liquid electrolytes results in a prohibitively low power density, a phenomenon that has made the commercialization of polymer electrolyte LMBs rare.[2] Some progress has been made using plasticizer in gel electrolytes,[5] but truly solid-state electrolytes are desired for safe, fast-charging, next-generation batteries.[6]

Finding polymer electrolyte with high room-temperature ionic conductivity has been a key engineering research focus for decades.[4,7] Electrolytes consisting of poly(ethylene oxide) (PEO) and the salt lithium bis(trifluoromethanesulfonyl)imide (LiTFSI) have been thoroughly studied.[8–10] Due to PEO's weak mechanical properties, particularly above its melting temperature

[a] *Department of Chemical and Biomedical Engineering, Florida A&M University-Florida State University (FAMU-FSU) College of Engineering, Tallahassee, FL 32310, USA. E-mail: dhallinan@eng.famu.fsu.edu*
[b] *Aero-propulsion, Mechatronics, and Energy Center, FAMU-FSU College of Engineering, Tallahassee, FL 32310, USA*

Table 1 Molecular structure of key polymer electrolyte components

Lithium bis(trifluoromethanesulfonyl)imide (LiTFSI)	Polystyrene-*block*-poly(ethylene oxide) (SEO)
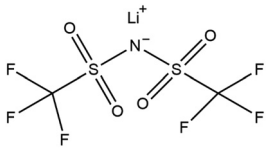	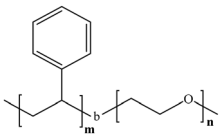

of roughly 67 °C, extensive research has been done on ion transport in microphase separated polystyrene (PS)-*block*-poly(ethylene oxide) (PS-*b*-PEO, SEO) block copolymers (BCPs).[11–14] The chemical structure of SEO and LiTFSI are shown in Table 1 for reference. The polystyrene block offers mechanical strength at the cost of being an insulator. In fact, ion transport occurs nearly exclusively through the PEO phase, particularly through percolated networks that enable a continuous path for the ions to travel across the electrolyte.

Due to poor miscibility between PS and PEO, SEO BCPs self-assemble into microstructures termed morphologies. These morphologies form spontaneously to minimize unfavorable enthalpic surface interactions between the PS and PEO monomers (by minimizing interfacial surface area) while entropy works as a competing force, seeking geometries that enable more chain conformations, *i.e.* minimize chain stretching.[15] The morphologies that achieve this energy minimization are a roughly discrete function of the volume fraction of each block.[9,15] As shown in Fig. 1, prior work on SEO BCP electrolytes with LiTFSI has reported that decreasing conductive domain size has a detrimental effect on ionic conductivity in lamellar BCPs.[16] On the other hand, hydrated single-ion conducting BCPs exhibited a weak increase in ionic conductivity with decreasing domain size,[17] and free polymer electrolytes loaded into track-etched membranes exhibited strong enhancement of ionic conductivity as they became more confined.[18,19] While this compilation of research results is interesting, it is not possible to infer the cause of this emergent physics due to the significant differences in material systems. Therefore, the present work focuses on a consistent set of SEO/LiTFSI BCP electrolytes with varying degrees of curvature and confinement. Ion transport and thermal properties have been measured in three unique morphologies: spheres (Sph), cylinders (Cyl), and lamellae (Lam). Two different samples are studied for each morphology; one that is PEO majority and another that is PS majority. Thus, a total of 6 different BCPs with varying degrees of confinement of the conductive PEO microphase are studied in this work.

A simple representation of the ionic conductivity of a composite with one conductive phase and one insulating phase developed from Sax and Ottino's work with effective medium theory (κ_{EM}) is shown in eqn (1).[9,20]

$$\kappa_{EM} = \frac{f}{\tau}\phi_c\kappa_c \quad (1)$$

This model considers the volume fraction of the conductive phase (ϕ_c), the probability that a morphological grain is conductive in the direction of ion transport as encapsulated by the morphology factor (f), and the tortuosity (τ) of conductive pathways, which is defined conventionally. Finally, κ_c represents the ionic conductivity of the pure conductive phase, in this case PEO/LiTFSI. Innate in this model is the assumption that the PEO block's proximity to PS does not fundamentally change its intensive properties. In other words, κ_c is assumed to be equal to that of a bulk PEO/LiTFSI electrolyte (where no PS is present). This work seeks to re-examine the ion transport and thermal properties of SEO by considering how confinement, the physical proximity and interfacial interaction between opposite phases, may affect the properties of the conductive phase, as compared to bulk PEO/LiTFSI homopolymer electrolyte. Fig. 2 shows values for the composite variable, $\frac{f}{\tau}$, whose values are taken from a 2018 review by Hallinan, Villaluenga, and Balsara.[9]

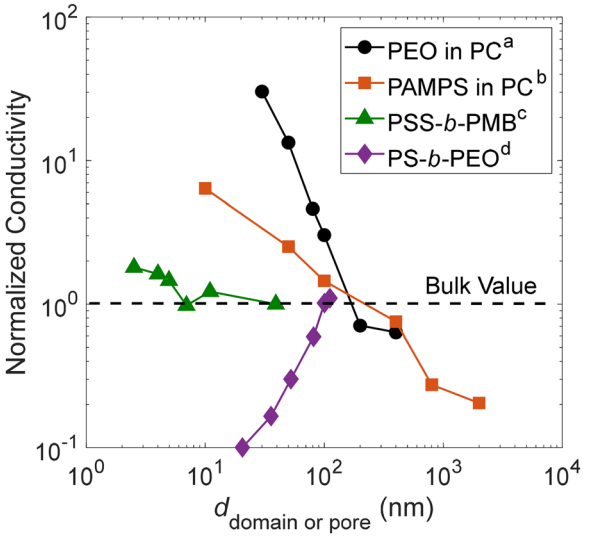

Fig. 1 Ionic conductivity of various nanostructured electrolytes normalized to bulk conductivity of the conducting phase. Below ~100 nm, nanoscale enhancement/impediment occurs in pores of PC and in BCP domains, demonstrating the possible effects of nanostructure on ion transport. PAMPS is a polyanion confined in nanopores, whereas PSS is a polyanion both confined in BCP cylindrical domains and tethered to the matrix. It is unknown if universal rules govern the effect of nanostructure on ion/molecule transport. [a] PEO + LiTFSI salt in polycarbonate (PC) pores.[18] [b] Poly(2-acrylamido-2-methyl-1-propanesulfonic acid) (PAMPS) in PC pores.[19] [c] Poly(styrenesulfonate-*block*-methylbutylene) (PSS-*b*-PMB).[17] [d] PS-*b*-PEO + LiTFSI.[16]

Experimental

Block copolymer synthesis

SEO block copolymers were synthesized using anionic polymerization, an excellent technique for fundamental polymer studies due to the control it grants over the molecular weight of each block as well as the low polydispersity of the product polymer.[21] PS was first synthesized from purified styrene with a *sec*-butyllithium initiator in benzene. The molecular weight of the PS was then determined *via* size exclusion chromatography.

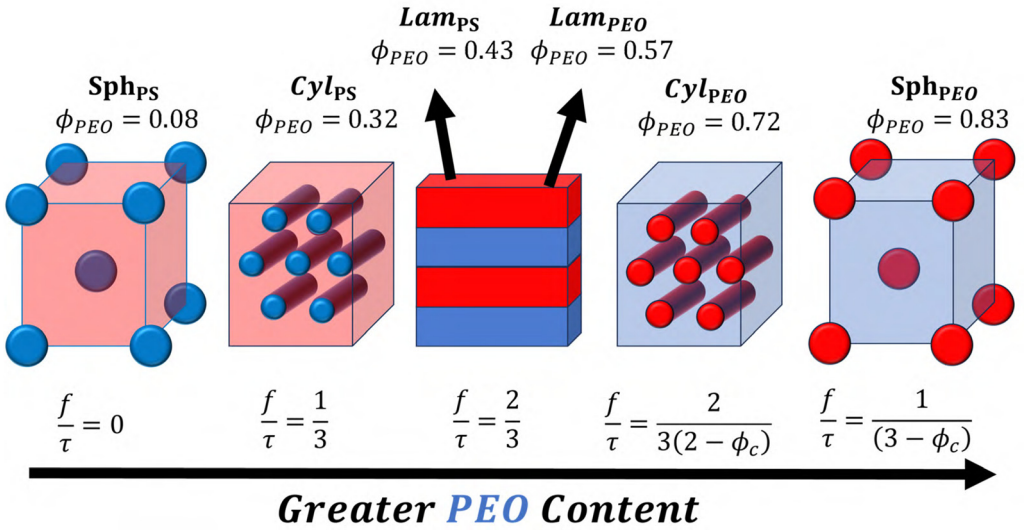

Fig. 2 Schematic representation of the morphological structure of each block copolymer in this study with its corresponding neat PEO volume fraction (ϕ_{PEO}). Red represents polystyrene while blue represents PEO. Spheres (Sph), cylinders (Cyl), and lamellae (Lam) of both PEO and PS are shown. The composite variable $\frac{f}{\tau}$ is discussed in greater detail in a 2018 review by Hallinan, Villaluenga, and Balsara.[9]

Purified ethylene oxide was grown on the end of the polystyrene with the aid of phosphonium catalyst. The polymerization was terminated with degassed methanol. Detailed synthetic steps can be found in works by Hadjichristidis and collaborators,[22] as well as Fetters and Morton.[21]

Electrolyte and neat BCP sample preparation for thermal and electrochemical characterization

SEO polymers were dried at 60 °C under vacuum for 24 h, while LiTFSI salt was dried at 120 °C for 48 h under vacuum. After drying, all materials were transferred into an argon-filled glovebox (less than 0.2 ppm of H_2O and O_2) without exposure to air (using a temperature-controlled antechamber) and maintained in an argon or inert vacuum environment unless explicitly noted. In the glovebox, approximately 1 gram of each polymer was combined with enough LiTFSI to achieve a molar ratio, $r = 0.085$ [mol Li] per [mol O]. Dimethylformamide (DMF) was added to make a 5 wt% solids solution that was mixed for approximately 16 h at 40 °C. Neat polymers were prepared with the same method, except that no salt was added.

Each solution was cast on a level plate set to 60 °C to drive off most of the solvent over a 16 h period and subsequently dried under vacuum at 90 °C for 24 hours. A small amount of each solution, enough to achieve ~8 mg of residual solids after DMF removal, was cast into aluminum pans for differential scanning calorimetry (DSC). After drying, the DSC pans were hermetically sealed for later testing. The bulk of each solution was cast onto nickel foil. In the case of PEO majority SEOs, free-standing membranes were not produced by this method due to the electrolyte's fragility, and these samples were transferred into glass vials for drying. PS majority SEOs formed robust membranes that were easily peeled from the nickel foil prior to vacuum drying. SEO/LiTFSI electrolytes were built into lithium symmetric cells for electrochemical characterization using previously established methods.[23,24] A polyethylene spacer was used for PEO majority SEOs to augment their mechanical strength while free standing membranes were used for PS majority SEOs.

Neat PEO (M_n = 20 kg mol^{-1}, Sigma-Aldrich), and neat polystyrene (M_n = 170 kg mol^{-1}, M_w = 350 kg mol^{-1}, Sigma-Aldrich) were prepared in the same fashion as the neat SEO samples and used as controls. Due to polystyrene's poor solubility in DMF, it was dissolved in chloroform prior to being cast on nickel foil in an air environment at 60 °C for 16 h. The sample was cast in air to enable the removal of chloroform before taking the sample into the glovebox, because halogenated solvent vapors irreversibly bind to and inactivate the catalyst in the glovebox's purification column that adsorbs water and oxygen from the argon gas. The polystyrene sample was peeled off the foil and dried in the glovebox antechamber at 90 °C for 24 h before it was taken into the glovebox. Excluding thermogravimetric analysis, neat and salt-containing polymers remained in an inert/dry environment following drying in the glovebox antechamber.

Thermogravimetric analysis (TGA) and differential scanning calorimetry (DSC)

Prior to studying the electrochemical properties and thermal transition behavior of each polymer or polymer electrolyte, TGA was employed to ensure the thermal stability of each species on relevant temperature ranges and testing environments. A dry nitrogen purged TA Instruments TGA Q50 was used for testing. Neat SEO polymers, polystyrene, and PEO were ramped from room temperature to 105 °C at 10 °C min^{-1} and held isothermally for 1 minute to drive off any absorbed water. The resulting mass after this 1-minute period was taken as the

polymer's initial mass which deviated by less than 0.5% from the initial mass. The TGA was then ramped to 600 °C at a ramp rate of 10 °C min^{-1} while the mass loss was tracked.

DSC was conducted to reveal variations in thermal transition behavior between differing SEOs as well as the effect of adding salt to each polymer. DSC began by holding each sample for 5 minutes isothermally at 210 °C for five minutes to erase thermal history (the highest expected thermal transition of either homopolymer is the T_g of polystyrene occurring at roughly 100 °C). After this, two heating and cooling cycles were completed with each cycle beginning with the sample being ramped to −60 °C at 20 °C min^{-1} followed by a 5-minute isothermal hold. Following this, the sample was ramped at the same rate to 210 °C and once again held isothermally for 5 minutes. This cycle was repeated once to ensure reproducibility in thermal properties, and data from the 2nd cycle is shown in each figure.

Small angle X-ray scattering

Small angle X-ray scattering (SAXS) on the neat copolymers was completed as part of a previous investigation at Argonne National Laboratory at the 8-ID-I beamline of the Advanced Photon Source.[25] Further details about this beamline and measurement techniques are reported by Sinha and collaborators,[25,26] and our previous study on BCP dynamics.[25] Neat SAXS samples were prepared as follows; the procedure is further detailed in our previous publication.[25] Approximately 500 mg of each SEO was dissolved in approximately 5 mL of toluene in an air environment. The mixture was stirred at 65 °C until a homogeneous solution was generated. The solution was cast in a stainless-steel dish of diameter 75 mm (VWR, model BOCH8636), with a lid placed on top of the dish leaving only a small space for solvent effluent to slow drying time. The dishes were maintained at 80 °C with a nitrogen purge for one week to allow solvent to evaporate. Afterwards, the dry membranes were removed from the dishes and dried under vacuum at 90 °C for 48 hours. Each membrane was then folded multiple times and pressed at 115 °C in a dry room (dew point −23 °F, ambient T 71 °F) using a Carver hot press applying a force of 1.6 MTon (equivalent to 1000 psi) for approximately 5 minutes. The thickness of the pressed membrane was checked to make sure it fell between 1 and 2 mm as is required for synchrotron hard X-ray measurements. Samples were then sealed in airtight stainless steel sample holders inside an argon glovebox to ensure an inert environment during X-ray exposure. Finally, all samples were annealed at 180 °C for 48 hours under vacuum. After transport to Argonne National Lab neat SEO samples were thermally equilibrated at 120 °C prior to SAXS measurements.

SEO/LiTFSI electrolytes for SAXS were cast and dried exactly as they were for electrochemical characterization (cast at 60 °C in an argon filled glovebox and subsequently dried under vacuum at 90 °C for 24 hours). Following drying, the electrolytes were pressed into SAXS sample holders prior to annealing at 180 °C for 48 hours under vacuum. Samples were then shipped to the National Synchrotron Light Source II at Brookhaven National Laboratory, where SAXS data were collected at beamline 11-ID at room temperature (as temperature control was not possible in the set-up available).

Electrochemical characterization

Lithium symmetric cells were used to measure the ionic conductivity (κ) and cation transference number (t_+) of each electrolyte using electrochemical impedance spectroscopy (EIS) and potentiostatic polarization, respectively. Symmetric cells were made using previously established methods.[23,24] Briefly, each electrolyte was placed (medially) between two pieces of lithium metal foil (MTI Corp). Nickel tabs (TOB New Energy) were used as current collectors and were placed on the lateral surface of each piece of lithium foil. Polyamide tape (McMaster-Carr) was used to secure each assembly to pouch material (MTI Corp) prior to vacuum sealing inside the glovebox to form an air-tight pouch cell. For the PEO majority block copolymers, a polyethylene spacer (ID = 6 mm, OD = 12 mm, thickness = 6 mm) was used to augment the electrolyte's mechanical strength. Free-standing membranes of the PS majority electrolytes were used to separate the lithium metal electrodes. The electrolyte membranes had diameter = 12 mm and thicknesses on the order of 200 μm with actual thickness of each cell measured and used for calculations. The lithium metal electrodes had diameter of 6 mm and thickness of 0.17 mm.

The κ of each SEO electrolyte was determined in lithium symmetric cells using EIS. An alternating voltage with peak amplitude of 10 mV was applied in a frequency range of 1 MHz to 100 mHz. Cells were given 1 h to return to electrochemical equilibrium between measurements. The EIS measurements were conducted from 90 to 30 °C in 10 °C descending increments. 25 °C was also measured to roughly simulate ambient conditions. Three replicates were conducted per temperature per cell. At least 3 cells of each composition were constructed and measured. Three hours were allowed for thermal equilibration after each temperature change.

The cationic transference number (t_+) was determined at 90 °C using the potentiostatic polarization method.[27,28] Each cell was polarized using chronoamperometry at 10 mV for 1 h, and the initial and steady state currents were determined. The initial and steady state resistances were also determined, using EIS with the settings described above. At least three measurements were taken on at least three cells of each sample type.

Results and discussion

For ease of discussion, Table 2 introduces an abbreviation system for each SEO tested in this study that reveals the expected morphologies to be studied in this work. These predictions are based on well-established relationships between PEO volume fraction (ϕ_{PEO}) and the theoretically predicted morphology for neutral diblock copolymers.[9,15] Additionally, the volume fraction of the PEO block after the addition of LiTFSI salt was approximated assuming simple volume additivity and is reported in Table 2. This volume fraction represents the

Table 2 PEO and conductive phase volume fractions, PEO weight fractions, block molecular weights, polydispersity index (Đ). Polymers are named according to their thermodynamically expected morphologies

Polymer[a]	ϕ_{PEO}	ϕ_c[b]	w_{PEO}	M_n (kg mol^{-1}) PS	PEO	Đ
SEO–Sph_{PS}	0.08	0.12	0.08	154	13.7	1.08
SEO–Cyl_{PS}	0.30	0.39	0.32	91.5	43.6	1.10
SEO–Lam_{PS}	0.42	0.52	0.44	149	117	1.06
SEO–Lam_{PEO}	0.51	0.61	0.54	122	141	1.04
SEO–Cyl_{PEO}	0.72	0.79	0.74	36.5	104	1.05
SEO–Sph_{PEO}	0.83	0.88	0.84	19.2	102	1.10

[a] SEO–X_Y is an abbreviation for each SEO where X is the expected morphology and Y is the majority species. [b] Conductive phase volume fraction for $r = 0.085$ mol_{LiTFSI} mol_{EO}^{-1}, assuming volume additivity and using component densities at 25 °C.

expected volume of the conductive phase (ϕ_c). This value was found by assuming the LiTFSI exclusively enters the PEO block and neither component changes specific volume upon mixing. An example ϕ_c calculation is shown in the SI in Appendix S5. This was done to demonstrate that, even in this most extreme case of PEO swelling, the expected morphology for each SEO remains the same. The number average molecular weight (M_n) of the PEO and PS blocks and the PEO mass fraction (w_{PEO}) are also reported in Table 2.

The thermal transitions of each neat polymer and polymer/LiTFSI electrolyte were studied. Nitrogen purged TGA was first employed on each neat polymer to ensure thermal stability within the desired testing range. The temperature at which a 5 wt% loss in sample mass was observed (T_D) was used as a heuristic to compare the relative thermal stability of each polymer. T_D is shown as a function of PEO volume fraction in Fig. 3. Fig. 3 shows that increasing PEO content in the BCP roughly correlates with decreased thermal stability. The variation in thermal stability is a relatively modest 27 °C with a maximum T_D of 362 °C occurring at 8 vol% PEO (PS majority spheres) and a minimum occurring at 335 °C for neat PEO. The neat PEO used in this work has a molecular weight (M_n) of 20 kg mol^{-1}, similar to the M_n of SEO–Sph_{PS} as is reported in Table S1. This indicates that the presence of PS, and perhaps its covalent attachment to the PEO chain end, has a stabilizing effect on thermal degradation. These TGA measurements indicate that DSC sweeps up to 210 °C are acceptable regarding thermal stability.

As was described in the Experimental section, a 20 °C min^{-1} ramp rate was employed to measure thermal transitions occurring during both polymer heating and cooling. DSC heating traces are shown in Fig. 4 for the neat polymers. Unsurprisingly, as the content of semicrystalline PEO increases, so too does the latent heat of fusion (ΔH_m). The maximum of the pure PEO melting endotherm occurs at 65.4 °C and the polymer is completely amorphous by approximately 70 °C. Above this temperature, every polymer will be amorphous, promoting ion movement *via* segmental mobility.[29,30] Interestingly, SEO–Sph_{PS} show no detectable crystallinity either due to poor signal-to-noise ratio or due to the amorphous PS block completely inhibiting crystallization.

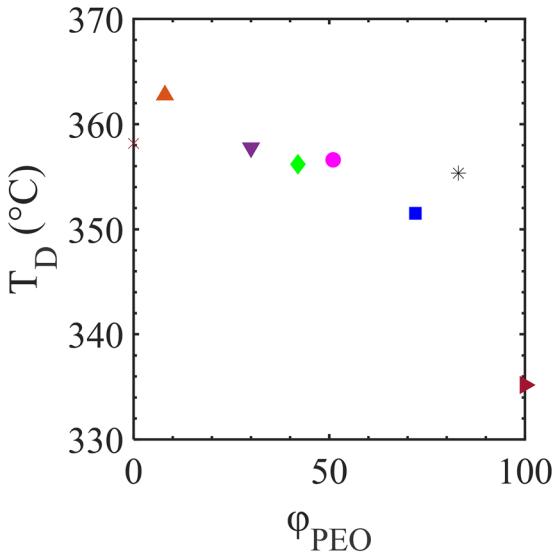

Fig. 3 Thermal decomposition temperature, T_D, (temperature at which 5 wt% mass loss was observed) of neat SEOs as a function of each neat block copolymer's volume fraction PEO (ϕ_{PEO}) as measured by N_2 purged thermogravimetric analysis. Neat PEO and PS homopolymers are shown for comparison. Each sample was ramped at 10 °C min^{-1} from 105 to 600 °C.

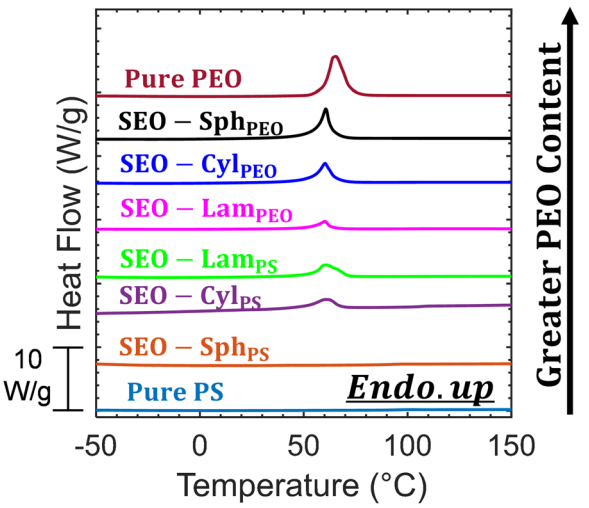

Fig. 4 DSC traces of neat SEO's. A heating ramp rate of 20 °C min^{-1} was used for all data sets.

Fig. 5 shows the effect of adding salt to each polymer (both PEO and SEO). Due to the immiscibility of PS and LiTFSI, the polystyrene sample shown in Fig. 5 is once again neat (and thus identical to Fig. 4). As has been reported previously, LiTFSI acts as a plasticizer, reducing the degree of crystallinity of the PEO phase as is visible through the reduced area under each endotherm.[31] Interestingly, moderate volume fractions corresponding to the cylindrical and lamellar morphologies show a less dramatic decrease in ΔH_m.

This is made even more apparent when the degree of crystallinity (χ_c) of the PEO block is calculated. This normalization is

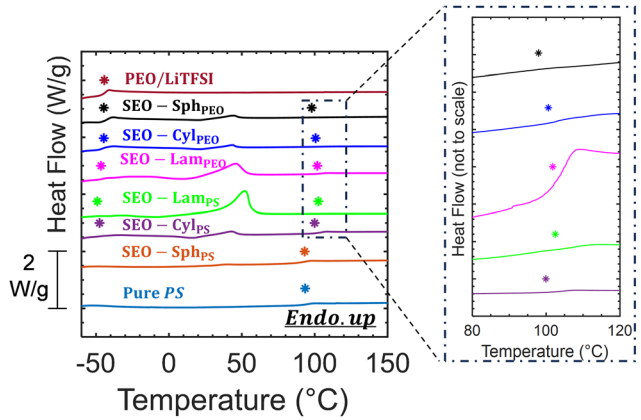

Fig. 5 DSC heating traces of SEO/LiTFSI and PEO/LiTFSI electrolytes. No salt was added to polystyrene due to immiscibility. A heating ramp rate of 20 °C min^{-1} was used. The window on the right is used to display otherwise visually subtle PS T_g.

essential as it controls for the sample mass contributed by the non-crystallizable component: PS. This normalization is done according to eqn (2),[32]

$$\chi_c = \frac{\Delta H_m}{w\Delta H_m^0} \times 100 \quad (2)$$

where χ_c is the degree of crystallinity per mass of the PEO block, ΔH_m^0 is the standard melting enthalpy of 100% crystalline PEO, w is the weight fraction of the PEO block in each SEO/LiTFSI electrolyte relative to the total mass of SEO and LiTFSI. Due to a wide variety of reported values, ΔH_m^0 was taken as 203 J g^{-1} based on an average of several reports as was compiled for a previous publication.[33–35] There are several remarkable features of the crystallinity results shown in Fig. 6A. First, the PEO-minority spheres exhibit no crystallinity, even in the absence of LiTFSI. In fact, all SEOs exhibit lower crystallinity than pure PEO, in agreement with prior reports.[36] Thus, physical confinement by polystyrene due to the BCP structure appears to play a role in inhibiting crystallization. Confinement effects on crystallization and ion transport will be discussed in more depth below, after SAXS results are discussed.

Regarding secondary phase transitions, only the salt doped copolymers showed two visible T_g values, and thus the electrolytes were used to probe the relationship between ϕ_c and T_g. In general, two T_g's were found for each SEO/LiTFSI electrolyte as shown in Fig. 5. One T_g is in proximity to −48 °C, the T_g of neat PEO as reported in a previous investigation.[24] The other T_g is similar to the value measured in this work for pure PS, 93.5 °C. PS majority spheres was the only polymer where only one T_g was detected. This is likely due to a weak PEO signal as a result of low PEO wt%. Fig. 6B shows that T_g was a very weak function of volume fraction PEO, and thus likely does not contribute considerably to variances in ion transport properties when the salt concentration is held constant.

Following thermal characterization, the ion transport properties of each electrolyte were measured. t_+ was probed using potentiostatic polarization at 90 °C. The red series in Fig. 7 is simply the ratio of the steady state current density (I_{ss}) and the initial current density (I_0) as shown in eqn (3).

$$t_{+,ss} = \frac{I_{ss}}{I_0} \quad (3)$$

This equation can be further refined by correcting for charge transfer resistance as proposed by Bruce, Vincent, and Evans and is shown in blue on Fig. 7.[28,37] This correction is shown in eqn (4),

$$t_+ = \frac{I_{ss}(\Delta V - I_0 R_0)}{I_0(\Delta V - I_{ss} R_{ss})} \quad (4)$$

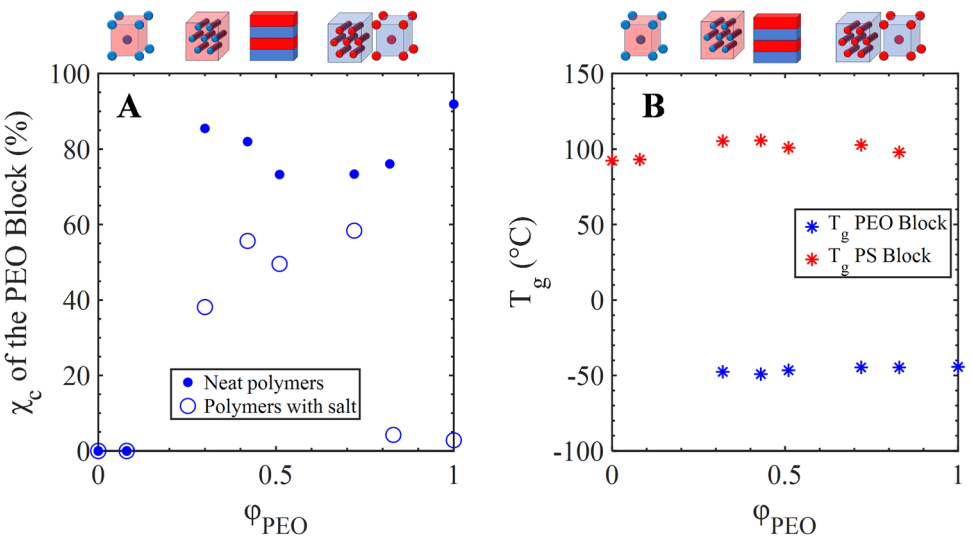

Fig. 6 (A) PEO mass normalized degree of crystallinity (χ_c) of neat polymers and with a LiTFSI ion concentration of r = 0.085 mol Li per mol O. (B) T_g of PEO/LiTFSI and SEO/LiTFSI electrolytes and neat PS. Results are shown as a function of PEO volume fraction (ϕ_{PEO}), *i.e.* that of neat SEO. The blue series corresponds to the lower T_g attributable to the PEO block while the red series corresponds to that of the higher T_g, attributable to the PS block. Schematics of the expected morphology of each SEO are shown above each data point.

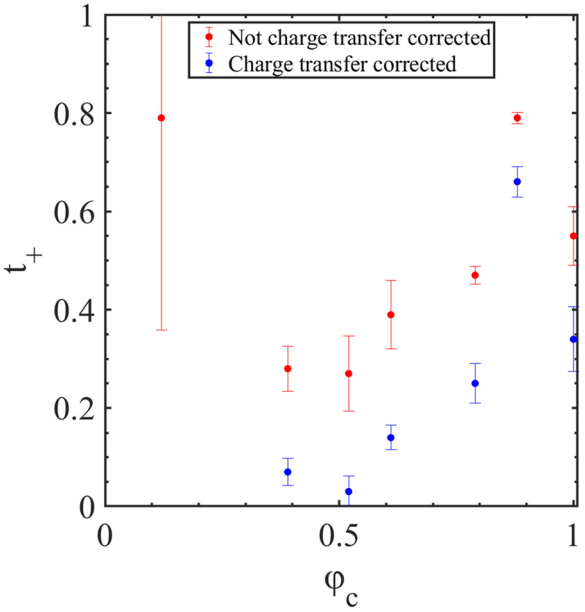

Fig. 7 Cation transference number (t_+) of SEO/LiTFSI electrolytes determined at 90 °C as calculated from eqn (3) (red) or eqn (4) (blue). For the lowest PEO volume fraction, the EIS data did not exhibit a feature associated with interfacial resistance, and a charge transfer corrected value is therefore not reported.

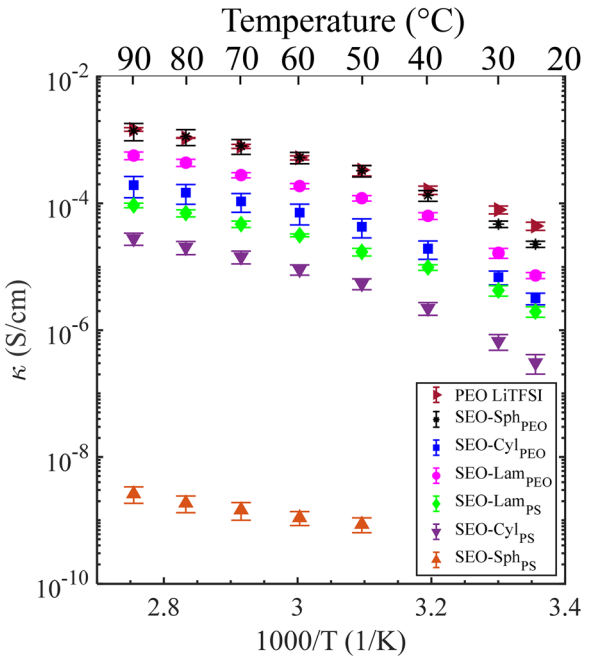

Fig. 8 Ionic conductivity (κ) of SEOs with LiTFSI salt with an ion concentration of r = 0.085 mol Li per mol O.

where R_0 is the unpolarized interfacial resistance, R_{ss} is the steady state interfacial resistance, and ΔV is the applied potential gradient. In both cases ($t_{+,ss}$ and t_+), the transference number has an unexpected dependence on PEO volume fraction, increasing with increasing ϕ_{PEO} to a value in SEO–Sph$_{PEO}$ that is greater than that in the homopolymer PEO electrolyte. We are not aware of prior reports that found transference number to depend on volume fraction of the block copolymer's conductive phase and note that electrochemical theory does not predict such a dependence, as transference number is a fractional mobility (of the cation in this case). Speculating on possible explanations, migration is related to the formation and build up of the ionic double layers at the electrodes, such that an orientational dependence of interfacial BCP structure at the lithium electrode could play a role in this dependence. Perpendicular alignment of BCP lamellar structure near a lithium electrode has been observed previously.[38] Another possibility is that confinement fundamentally changed the conductive phase properties, perhaps by interfering with the ability of PEO to strongly coordinate Li^+, rendering the lithium ions more mobile and resulting in increased cation transference number. This possibility is investigated in semi-quantitative fashion below using other conductive phase properties, and we refrain from assigning a specific physical cause to this dependence of t_+ on ϕ_{PEO}.

κ of the SEO/LiTFSI electrolytes as a function of temperature is shown *via* an Arrhenius plot in Fig. 8. Of note in this figure is the relative parity between SEO–Sph$_{PEO}$ and PEO/LiTFSI, particularly at high temperatures. Furthermore, SEO–Sph$_{PS}$ shows a non-zero κ which disagrees with the simple prediction of eqn (1). This is because eqn (1) relies on the assumptions that PS is a perfect insulator and therefore no continuous path exists between the ionically conductive PEO/LiTFSI spheres. To verify the validity of treating PS as an insulator, the conductivity of pure PS was measured to be on the order of 10^{-18} S cm^{-1} at 90 °C. While it is difficult to verify if this measured PS conductivity corresponds to the transport of electrons or ions, it validates the assumption that ion transport through the PS domain can be neglected. The larger than expected ionic conductivity of SEO–Sph$_{PS}$ electrolyte may be due to disorder in the microphase separation enabling continuous paths for ions, *e.g. via* conduction through grain boundaries that are a known contributor to ion conduction.[39]

As was previously mentioned, each polymer is fully amorphous, even in the neat state, at and above about 60 °C. This means that data from 60 °C and above can be treated with classical models that capture the temperature dependence of ionic conductivity: the Arrhenius model and the Vogel–Fulcher–Tammann (VFT) model. The Arrhenius model is defined as:

$$\kappa(T) = \kappa_0 e^{-\frac{E_{a,Arrhenius}}{RT}} \quad (5)$$

Here, κ_0 is the preexponential factor representing the conductivity in the limit of infinite temperature, $E_{a,Arrhenius}$ is the Arrhenius activation energy, and R is the gas constant.[40] Similarly, the VFT model can be stated as:

$$\kappa(T) = \kappa_0 e^{\left(-\frac{B}{T-T_0}\right)} = \kappa_0 e^{\left(-\frac{E_{a,VFT}}{R(T-T_0)}\right)} \quad (6)$$

Here, $B = \frac{E_{a,VFT}}{R}$ and T_0 is the Vogel temperature and will be defined as 50 °C below the electrolyte's T_g, as per convention.[30,40] The T_g, of the PEO/LiTFSI electrolyte was found to be −46.7 °C; thus T_0 = 176.5 K. Due to the nonlinear nature of

this model, it is important to fix T_0 before regressing the other two parameters, in order to minimize compensation effects and obtain reproducible fit results. It was confirmed that the convention ($T_0 = T_g - 50$ K) agrees well with regressions in which T_0 was treated as an adjustable parameter, but those regressions resulted in much greater uncertainty in the values of the other two parameters and are therefore not reported.

In both models, the activation energy describes the negative of the slope of $\kappa(T^{-1})$ on a semilog plot and thus describes the rate of increase of κ with increasing temperature. The average and relative uncertainty of each activation energy was 34.5 kJ mol^{-1} ± 9.5% for $E_{a,Arrhenius}$ and 7.91 kJ mol^{-1} ± 11% for $E_{a,VFT}$, with the relative uncertainty defined as the quotient of the standard deviation and the average E_a multiplied by 100%. These values compare closely to the $E_{a,VFT}$ = 7.6 ± 7% kJ mol^{-1} found by Pesko and collaborators,[41] and $E_{a,Arrhenius}$ = 26.05 ± 3.7% kJ mol^{-1} found by Bakar and coworkers.[42] In both cases the activation energy is for homogeneous PEO/LiTFSI electrolytes with nearly the same salt concentration as this study. The VFT model's lower E_a can be attributed to the equation's empirical nature where $\kappa_{0,VFT}$ and $E_{a,VFT}$ are positively correlated *via* the compensation effect.[40] As E_a roughly corresponds to the temperature dependence of each electrolyte's conductivity, the self-consistency of $E_{a,Arrhenius}$ and $E_{a,VFT}$ suggest the PEO phase's ionic conductivity shows a similar dependence on temperature regardless of ϕ_c. This is shown in the Fig. S1 (in Appendix S1) where each SEO electrolyte's $\kappa(T)$ is normalized relative to the value at 90 °C. Normalized $\kappa(T)$ data collapse on a master curve down to 60 °C, below which different levels of crystallinity cause scatter. κ_0 showed much greater variation for both models due to the vastly different κ of each SEO. Fitting parameters for the Arrhenius model for each electrolyte are visible in Table S2 while VFT fitting parameters are shown in Table S3.

To demonstrate differences in κ and thus κ_0 between different SEOs, κ at 90 °C was plotted in Fig. 9 as a function of conductive phase volume fraction, ϕ_c. Fig. 9 demonstrates the non-monotonic relationship between ϕ_c and κ despite their generally direct correlation. SEO–Lam$_{PEO}$ is the sole contradiction to monotonicity as it shows a higher κ than the more PEO rich SEO–Cyl$_{PEO}$. Fig. 9 shows the predicted conductivity of each electrolyte according to the Sax and Ottino model (eqn (1)) as a blue line. In other words, the blue line in Fig. 9 is the effective-medium prediction of the κ of randomly oriented grains of simple body-centered-cubic, hexagonally packed cylinders, and lamellae. Conversely, the volume-weighted average ionic conductivity (κ_v) is also plotted in Fig. 9 and is shown in eqn (7). Eqn (7) can be simplified to a single term if the insulating polystyrene block's ionic conductivity (κ_{ins}) is approximately 0. Both versions of eqn (7) produce visually identical versions of the orange trace on Fig. 9.

$$\kappa_v = \kappa_c\phi_c + \kappa_{ins}\phi_{ins} = \kappa_c\phi_c \quad (7)$$

κ_v represents a homogenous and disordered electrolyte as is seen above the order-to-disorder temperature (T_{ODT}) of a BCP.[15] It should be noted that previous works have shown each of

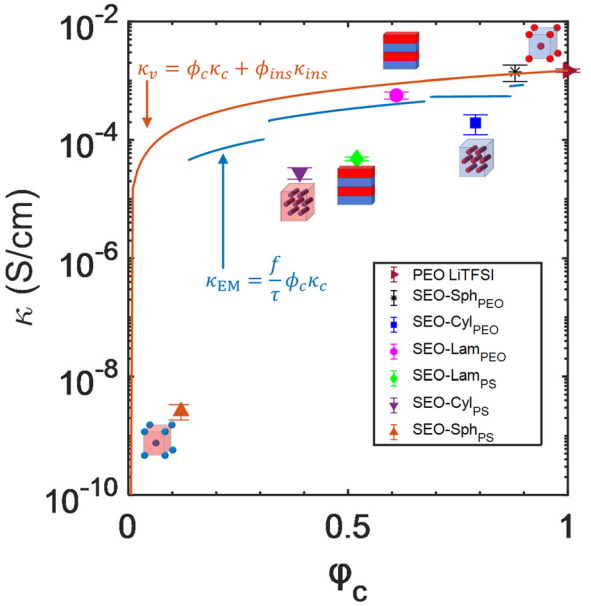

Fig. 9 Measured and predicted ionic conductivities of SEOs with salt at 90 °C (r = 0.085 mol$_{LiTFSI}$ mol$_{EO}^{-1}$). The blue line represents the effective medium prediction, κ_{EM} (eqn (1)), in which SEO–Sph$_{PS}$ is approximated as a perfect insulator. The orange line represents a simple volume-weighted average model of the conductivity, κ_v (eqn (7)), of PEO/LiTFSI and polystyrene at 90 °C. The equations for each of these models are shown in blue and orange on the figure, respectively.

these SEO morphologies is below T_{ODT} at 90 °C, and thus the observed data's negative deviation from the volume weighted average should be expected.[25,43,44] However, deviation below the Sax and Ottino model suggests a more complicated framework is likely needed. Reviewing Fig. 6A, the crystallinity of lamellar and cylindrical morphologies showed relatively low depression of the χ_c of their PEO blocks thus showing these morphologies have both complex ionic and thermal properties.

Due to the complexity of each of these results at least when cast as a function ϕ_c, SAXS data was leveraged to understand important dimensions in the BCP morphology (including the PEO/PS interfacial area per unit volume as derived in Appendix S3 in the SI). The one-dimensional SAXS patterns for the neat SEOs and SEO electrolytes are shown in the SI in Appendix S2. The primary scattering peak (q^*) is indicated on each of these profiles, as are up to three higher order peaks. Combined, broad peaks at high q-values are not labeled and are due to PEO crystals and poor long-range order that results from high molecular weight BCPs such as these being kinetically trapped during solvent casting with extremely slow structural evolution during thermal annealing.[22,36] From these SAXS profiles, the domain size (d) of each SEO was determined from q^*. Table 3 shows d and its relationship to q^* for each morphology. Prior work using real-space techniques (atomic force and electron microscopy) verifies that these BCPs exhibit the assigned morphology.[25,45] The addition of salt increases contrast (and possibly segregation strength) between the salt-containing PEO phase and PS, as indicated by improved signal to noise in salt-containing samples and in agreement with other work.[36,46–48]

Table 3 Domain spacing (d) and confinement length (c) values in neat BCPs and BCP electrolytes (r = 0.085 mol_{LiTFSI} mol_{EO}^{-1}), and schematic depicting physical description of c. In the schematics, red represents PS and blue represents PEO

Morphology	d and c (nm)		Schematic definition of c
	Neat (120 °C)	Electrolytes (RT)[a]	
SEO–Sph_{PS}	d = 45.9 c = 13.8	d = 35.7 c = 12.3	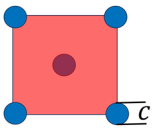
SEO–Sph_{PEO}	d = 42.1 c = 10.0	d = 34.0 c = 9.5	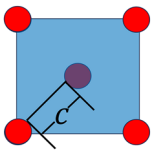
SEO–Cyl_{PS}	d = 94.2 c = 54.2	d = 125.1 c = 82.0	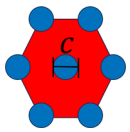
SEO–Cyl_{PEO}	d = 88.0 c = 39.3	d = 99.0 c = 51.6	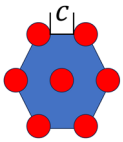
SEO–Lam_{PS}	d = 108.3 c = 45.5	—	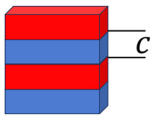
SEO–Lam_{PEO}	—	d = 163.9 c = 100.1	

[a] RT = room temperature.

A confinement length (c) was defined as the shortest distance between two non-conductive PS microdomains. Confinement length thus quantifies the bottleneck that limits transport/crystallization in the conductive phase. As the confinement length increases the conductive phase may be less influenced by the presence of the PS microdomains and thus may behave more similarly to an equivalent homopolymer PEO/LiTFSI electrolyte (as is assumed in eqn (1)). In the limit as c gets large, a microphase separated electrolyte would tend to the effective medium prediction. In the SI, the distance describing the confinement length for each SEO is shown in Appendix S4, and values of c for each SEO are shown in Table S1.

Fig. 10A shows χ_c as a function of confinement length. At the largest confinement length the PEO block is least confined by PS and the degree of crystallinity approaches the value in pure PEO (dashed line). With decreasing confinement length, χ_c decreases following saturated exponential growth (red curve). At these cooling rates, the effect of confinement is dramatic, and the characteristic length scale for the decay of χ_c is 15 nm. Confinement has been shown in numerous reports to reduce the rate of crystallization of BCP that contain an amorphous block, due in part to reduction in chain mobility but primarily due to nucleation becoming the rate limiting step.[49–51] In other words, when the confinement length is similar to the characteristic PEO crystal lamellae thickness (for rapid cooling that results in non-integer folding this is 12 nm)[22,52] a transition from heterogeneous to homogeneous nucleation occurs.[53] In our work, the decreased χ_c observed at low confinement lengths is a result of this slower rate of crystallization. The key length scale in our work agrees reasonably well with the literature reports and indicates that at our cooling rate of 20 °C min^{-1} there is a dramatic reduction in crystallization rate at confinements of 15 nm. There is a complex dependence of BCP crystallization rate on block molecular weight, number of blocks, and confinement length.[51,54,55] Studies with similar confinement lengths to our work have reported a transition from heterogeneous nucleation and growth dominated kinetics

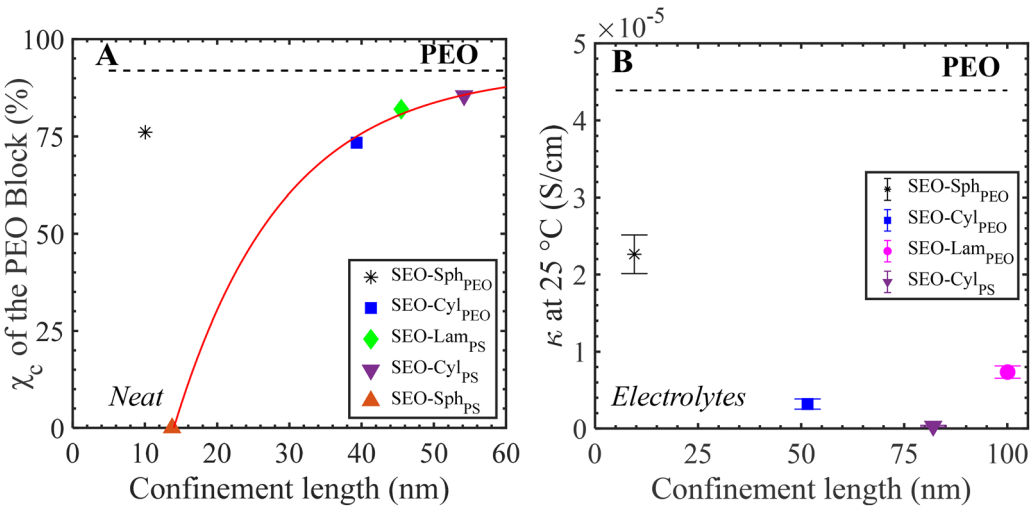

Fig. 10 (A) PEO mass normalized degree of crystallinity (χ_c) of neat polymers as a function of confinement length (c). c was calculated according to room temperature SAXS data in Appendix S2. The black dashed line is the value for pure PEO, and the red curve is a saturated exponential growth curve. (B) Measured ionic conductivities (κ) of SEOs with a salt concentration of r = 0.085 mol Li per mol O at 25 °C as a function of confinement length. The black dashed line is the value for PEO + LiTFSI electrolyte at the same temperature and salt concentration.

in the bulk to homogeneous nucleation that limits kinetics in confinement.[49,50] This also causes changes to PEO crystal orientation that have been observed in PS-*b*-PEO BCPs across a similar range of confinement to our study in both minority- and majority-PEO cylinders.[56,57] It is worth noting that the confinement effect does not capture the behavior of the spherical morphology with PEO majority in our work. Intuitively, the concept of confinement when PS spheres are nothing more than inclusions in a sea of PEO seems inappropriate in this case. Another consideration is the dimensionality of the confinement,[54] *e.g.* some studies report bulk crystallite-growth-like behavior in lamellar morphology but confined growth in cylindrical BCPs,[58] but other reports observe rate inhibition in lamella as well.[59] Finally, topological constraints are also at play in BCPs, where the tethering of the semicrystalline block to the glassy block also appears to contribute to impeding crystallization.[59,60]

These complex relationships reveal the need to advance effective medium theory predictions beyond a geometric description of the BCP (as captured by $\frac{f}{\tau}$) to a model that considers how confinement affects the properties of the conductive phase as compared to an analogous homopolymer electrolyte. To that end, we examine the dependence of BCP electrolyte conductivity on confinement length in Fig. 10B. SEO–Sph$_{PS}$ was neglected due to its lack of a continuous pathway for ions. Holistically considering all morphologies, κ appears to have a nonmonotonic dependence on c, with enhancement occurring with increasing confinement. However, regardless of confinement effects, the κ of BCP electrolytes is considerably lower than the homopolymer PEO electrolyte (dashed line), due in large part to the presence of nonconductive PS and concomitant tortuosity, both of which are captured by effective medium theory.

Conclusions

This study demonstrated the complex relationship between the volume fraction of each block and the thermal and ion transport properties of block copolymers. Effective medium theory considers the geometric features of each self-assembled morphology but it does not consider how the incorporation of PEO into a block copolymer might alter the conductive phase's thermal and ionic properties. A simple parameter, the confinement length, was introduced as a proxy for the relative strength of these confinement effects that evoke a divergence in behavior of the conductive phase from that exhibited in the bulk. In order to visualize the divergence from bulk behavior, we present normalized conductivity in Fig. 11, where the BCP electrolyte conductivity is normalized by that of PEO electrolyte at the same temperature and salt concentration. This normalization allows a large number of literature reports at various conditions to be directly presented along with the results of this work. For clarity, and due to apparent differences in behavior, only lamellar morphologies are reported in Fig. 11A and morphologies with curvature are reported in Fig. 11B. A general direct correlation was found between κ and c for the lamellar BCPs as can be seen in Fig. 11A, such that confinement is detrimental to transport in this morphology. This explains the unexpected early result in the area of BCP electrolytes, where lamellar BCP conductivity increased with increasing PEO block molecular weight (M_w),[61] *i.e.* d increases with increasing M_w, which reduces confinement. Conversely, a more complex relationship was found for cylinders (and possibly spheres), whereby confinement may be beneficial, *i.e.* κ increases with decreasing c, as shown in Fig. 11B. Fig. 11B also shows that while not sufficient on its own, effective medium theory does elucidate some key realities of transport in composite

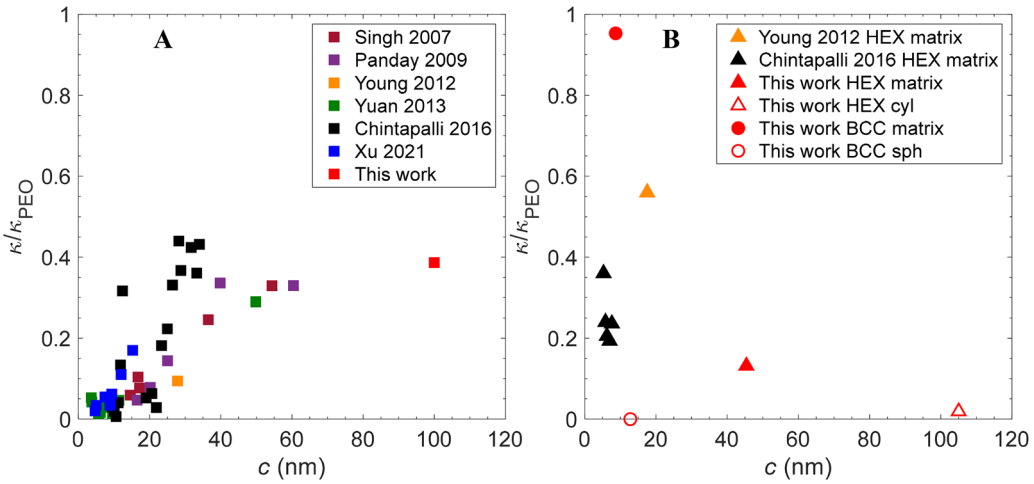

Fig. 11 Conductivity of SEO BCP electrolytes from literature and this work normalized to PEO electrolyte conductivity at the same salt concentration and temperature *versus* the confinement length, as defined in this work. (A) Lamellar (■) morphology designated in legend by first author and year: Singh, *et al.* 2007,[61] Panday, *et al.* 2009,[16] Young, *et al.* 2012,[62] Yuan, *et al.* 2013,[63] Chintapalli, *et al.* 2016,[43] Xu, *et al.* 2021,[64] and this work. (B) Hexagonally (HEX) packed cylinder matrix conductivity (▲) from Young, *et al.* 2012,[62] Chintapalli, *et al.* 2016,[43] and this work, and HEX cylinder (cyl) conductivity from this work (△), as well as body-centered cubic (BCC) sphere matrix conductivity with continuous PEO phase (●) and BCC spere (sph) conductivity with isolated PEO phase (○) both from this work.

electrolytes. For instance, the near zero ionic conductivity of SEO–Sph_{PS} shows the importance of a continuous pathway for ions to travel for meaningful ion conduction, as the continuous morphologies in Fig. 11B demonstrate. However, in contrast to polymer electrolytes confined in pores that can exhibit conductivity enhancement beyond that of the bulk (Fig. 1), BCPs universally appear to exhibit a reduction in conductivity with addition of non-conductive phase, including in minority PEO BCP electrolytes that have been first reported in this work. This may be due to differences in how conductivity was calculated in literature reports *versus* this work in which the macroscopic electrolyte area was used. Future work should focus on studying how changing c within the same geometry and BCP chemistry impacts the crystallization and transport properties of the conductive phase, as well as examining how BCP properties are affected by confinement in gyroid and other exotic morphologies.

Surprisingly, the transference number was found to increase with increasing PEO volume fraction. It is unclear if this is due to interfacial BCP structure at the electrode interface, confinement, or some other effect, but further investigation is warranted. The other properties of the block copolymers did not exhibit clear trends with PEO volume fraction, nor was the ionic conductivity of the electrolytes well represented by effective medium theory, which prompted the confinement analysis. Confinement clearly impedes crystallization, with a saturated exponential decay in degree of crystallinity at a confinement length of 15 nm. Confinement was found to decrease ionic conductivity in lamellar morphologies, with values approaching that predicted by effective medium theory in the limit of large confinement length (*i.e.* less confined). On the other hand, conductivity increased strongly with decreasing confinement length in curved morphologies (spheres and cylinders). In these morphologies with curvature, it is possible that confinement driven deviation of conductivity from bulk behavior could lead to unprecedented polymer electrolyte ion transport capability, an essential component in the quest for all-solid-state batteries. It remains to be seen if the deviation of the confined conductive phase from bulk behavior could lead to conductivity values surpassing even the effective-medium prediction and enable solid-state batteries.

Conflicts of interest

There are no conflicts of interest to declare.

Data availability

All data generated or analysed during this study are included in this published article and its supplementary information (SI). Supplementary information is available. See DOI: **https://doi.org/10.1039/d5sm00554j**.

Acknowledgements

This work was sponsored in part by the U.S. Department of Energy (DOE), Office of Energy Efficiency and Renewable Energy (EERE) in the Vehicle Technologies Office (VTO) through the Advanced Battery Materials Research (BMR) Program, managed by Simon Thompson and Tien Duong. It was also funded in part by a grant from the Florida State University President's SCS Program. For assistance with SAXS measurements, the authors thank Dr Subramanian Ramakrishnan, Dr Lutz Wiegart, Dr Omar Taleb, Dr Suresh Narayanan, and Dr Qingteng Zhang. This research used beamline 8-ID-I of the Advanced Photon Source, a DOE Office of Science user facility operated for the DOE Office of Science by Argonne National Laboratory under Contract No. DE-AC02-06CH11357, and beamline 11-ID of the National Synchrotron Light Source II, a DOE Office of Science User Facility operated for the DOE Office of Science by Brookhaven National Laboratory under Contract No. DE-SC0012704.

References

1 G. G. Njema, R. B. O. Ouma and J. K. Kibet, *J. Renewable Energy*, 2024, **2024**, 2329261, DOI: **10.1155/2024/2329261**.
2 J. B. Goodenough and Y. Kim, *Chem. Mater.*, 2010, **22**, 587–603, DOI: **10.1021/cm901452z**.
3 S. Choudhury, A. Agrawal, S. Wei, E. Jeng and L. A. Archer, *Chem. Mater.*, 2016, **28**, 2147–2157, DOI: **10.1021/acs.chemmater.6b00029**.
4 D. T. Hallinan, Jr. and N. P. Balsara, in *Annual Review of Materials Research*, ed. D. R. Clarke, 2013, vol. 43, pp. 503–525, DOI: **10.1146/annurev-matsci-071312-121705**.
5 A. R. Polu, K. Kim, A. A. Kareem, D. Kim, S. Song, S. V. Savilov and P. K. Singh, *J. Power Sources*, 2025, **625**, 235742, DOI: **10.1016/j.jpowsour.2024.235742**.
6 P. Albertus, V. Anandan, C. Ban, N. Balsara, I. Belharouak, J. Buettner-Garrett, Z. Chen, C. Daniel, M. Doeff, N. J. Dudney, B. Dunn, S. J. Harris, S. Herle, E. Herbert, S. Kalnaus, J. A. Libera, D. Lu, S. Martin, B. D. McCloskey, M. T. McDowell, Y. S. Meng, J. Nanda, J. Sakamoto, E. C. Self, S. Tepavcevic, E. Wachsman, C. Wang, A. S. Westover, J. Xiao and T. Yersak, *ACS Energy Lett.*, 2021, **6**, 1399–1404, DOI: **10.1021/acsenergylett.1c00445**.
7 D. E. Fenton, J. M. Parker and P. V. Wright, *Polymer*, 1973, **14**, 589, DOI: **10.1016/0032-3861(73)90146-8**.
8 D. Pesko, *Doctor of Philosophy*, U.C. Berkeley, 2018.
9 D. T. Hallinan, I. Villaluenga and N. P. Balsara, *MRS Bull.*, 2018, **43**, 759–767, DOI: **10.1557/mrs.2018.212**.
10 M. P. Blatt and D. T. Hallinan, *Ind. Eng. Chem. Res.*, 2021, **60**, 17303–17327, DOI: **10.1021/acs.iecr.1c02938**.
11 M. D. Galluzzo, W. S. Loo, A. A. Wang, A. Walton, J. A. Maslyn and N. P. Balsara, *J. Phys. Chem. B*, 2020, **124**, 921–935, DOI: **10.1021/acs.jpcb.9b11066**.
12 S. A. Mullin, G. M. Stone, A. Panday and N. P. Balsara, *J. Electrochem. Soc.*, 2011, **158**, A619–A627, DOI: **10.1149/1.3563802**.
13 K. J. Harry, D. T. Hallinan, D. Y. Parkinson, A. A. MacDowell and N. P. Balsara, *Nat. Mater.*, 2014, **13**, 69–73, DOI: **10.1038/nmat3793**.
14 K. J. Harry, D. Y. Parkinson and N. P. Balsara, *J. Visualized Exp.*, 2015, **102**, 53021, DOI: **10.3791/53021**.

15 Y. Mai and A. Eisenberg, *Chem. Soc. Rev.*, 2012, **41**, 5969–5985, DOI: 10.1039/C2CS35115C.
16 A. Panday, S. Mullin, E. D. Gomez, N. Wanakule, V. L. Chen, A. Hexemer, J. Pople and N. P. Balsara, *Macromolecules*, 2009, **42**, 4632–4637, DOI: 10.1021/ma900451e.
17 M. J. Park, K. H. Downing, A. Jackson, E. D. Gomez, A. M. Minor, D. Cookson, A. Z. Weber and N. P. Balsara, *Nano Lett.*, 2007, **7**, 3547–3552, DOI: 10.1021/nl072617l.
18 S. Vorrey and D. Teeters, *Electrochim. Acta*, 2003, **48**, 2137–2141, DOI: 10.1016/s0013-4686(03)00196-8.
19 H. Chen, G. R. Palmese and Y. A. Elabd, *Chem. Mater.*, 2006, **18**, 4875–4881, DOI: 10.1021/cm061422w.
20 J. Sax and J. M. Ottino, *Polym. Eng. Sci.*, 1983, **23**, 165–176, DOI: 10.1002/pen.760230310.
21 M. Morton and L. J. Fetters, *Rubber Chem. Technol.*, 1975, **48**, 359–409, DOI: 10.5254/1.3547458.
22 O. Oparaji, X. Zuo and D. T. Hallinan, *Polymer*, 2016, **100**, 206–218, DOI: 10.1016/j.polymer.2016.08.026.
23 M. D. Berliner, B. C. McGill, M. Majeed and D. T. Hallinan, *J. Electrochem. Soc.*, 2019, **166**, A297–A304, DOI: 10.1149/2.0851902jes.
24 N. Nguyen, M. P. Blatt, K. Kim, D. Hallinan and J. G. Kennemur, *Polym. Chem.*, 2022, **13**, 4309–4323, DOI: 10.1039/D2PY00605G.
25 O. Taleb, M. P. Blatt, V. Signorini, O. Oparaji, K. Kim, E. Lochner, S. Narayanan, Q. Zhang and D. Hallinan Jr, *Macromol. Chem. Phys.*, 2024, **225**, 2300357, DOI: 10.1002/macp.202300357.
26 S. K. Sinha, Z. Jiang and L. B. Lurio, *Adv. Mater.*, 2014, **26**, 7764–7785, DOI: 10.1002/adma.201401094.
27 P. G. Bruce, J. Evans and C. A. Vincent, *Solid State Ionics*, 1987, **25**, 255–262, DOI: 10.1016/0167-2738(87)90189-5.
28 S. Zugmann, M. Fleischmann, M. Amereller, R. M. Gschwind, H. D. Wiemhofer and H. J. Gores, *Electrochim. Acta*, 2011, **56**, 3926–3933, DOI: 10.1016/j.electacta.2011.02.025.
29 D. Golodnitsky, E. Strauss, E. Peled and S. Greenbaum, *J. Electrochem. Soc.*, 2015, **162**, A2551, DOI: 10.1149/2.0161514jes.
30 Z. Li, J. Fu, X. Zhou, S. Gui, L. Wei, H. Yang, H. Li and X. Guo, *Adv. Sci.*, 2023, **10**, 2201718, DOI: 10.1002/advs.202201718.
31 M. Marzantowicz, J. R. Dygas, F. Krok, J. L. Nowinski, A. Tomaszewska, Z. Florjanczyk and E. Zygadlo-Monikowska, *J. Power Sources*, 2006, **159**, 420–430, DOI: 10.1016/j.jpowsour.2006.02.044.
32 K. Kim, N. Nguyen, S. F. Marxsen, S. Smith, R. G. Alamo, J. G. Kennemur and D. T. Hallinan Jr, *Macromol. Chem. Phys.*, 2021, **222**, 2100269, DOI: 10.1002/macp.202100269.
33 A. R. Polu, H.-W. Rhee and D. K. Kim, *J. Mater. Sci.: Mater. Electron.*, 2015, **26**, 8548–8554, DOI: 10.1007/s10854-015-3527-9.
34 E. Salmon, S. Guinot, M. Godet and J. F. Fauvarque, *J. Appl. Polym. Sci.*, 1997, **65**, 601–607, DOI: 10.1002/(SICI)1097-4628(19970718)65:3<601::AID-APP20>3.0.CO;2-Y.
35 G. Zardalidis, J. Mars, J. Allgaier, M. Mezger, D. Richter and G. Floudas, *Soft Matter*, 2016, **12**, 8124–8134, DOI: 10.1039/C6SM01622G.
36 O. Oparaji, S. Narayanan, A. Sandy, S. Ramakrishnan and D. Hallinan, *Macromolecules*, 2018, **51**, 2591–2603, DOI: 10.1021/acs.macromol.7b01803.
37 P. G. Bruce and C. A. Vincent, *J. Electroanal. Chem. Interfacial Electrochem.*, 1987, **225**, 1–17, DOI: 10.1016/0022-0728(87)80001-3.
38 G. M. Stone, S. A. Mullin, A. A. Teran, D. T. Hallinan, Jr., A. M. Minor, A. Hexemer and N. P. Balsara, *J. Electrochem. Soc.*, 2012, **159**, A222–A227, DOI: 10.1149/2.030203jes.
39 L. S. Grundy, S. Fu, M. D. Galluzzo and N. P. Balsara, *Macromolecules*, 2022, **55**, 10294–10301, DOI: 10.1021/acs.macromol.2c01837.
40 K. M. Diederichsen, H. G. Buss and B. D. McCloskey, *Macromolecules*, 2017, **50**, 3831–3840, DOI: 10.1021/acs.macromol.7b00423.
41 D. M. Pesko, Y. Jung, A. L. Hasan, M. A. Webb, G. W. Coates, T. F. Miller and N. P. Balsara, *Solid State Ionics*, 2016, **289**, 118–124, DOI: 10.1016/j.ssi.2016.02.020.
42 R. Bakar, S. Darvishi, U. Aydemir, U. Yahsi, C. Tav, Y. Z. Menceloglu and E. Senses, *ACS Appl. Energy Mater.*, 2023, **6**, 4053–4064, DOI: 10.1021/acsaem.3c00310.
43 M. Chintapalli, T. N. P. Le, N. R. Venkatesan, N. G. Mackay, A. A. Rojas, J. L. Thelen, X. C. Chen, D. Devaux and N. P. Balsara, *Macromolecules*, 2016, **49**, 1770–1780, DOI: 10.1021/acs.macromol.5b02620.
44 H. Xu, E. M. Greve and M. K. Mahanthappa, *Macromolecules*, 2019, **52**, 5722–5734, DOI: 10.1021/acs.macromol.9b00900.
45 V. Signorini, O. Taleb, M. G. Baschetti, M. Minelli and D. T. Hallinan, *Polymer*, 2025, **333**, 128637, DOI: 10.1016/j.polymer.2025.128637.
46 N. J. Shah, S. Dadashi-Silab, M. D. Galluzzo, S. Chakraborty, W. S. Loo, K. Matyjaszewski and N. P. Balsara, *Macromolecules*, 2021, **54**, 1414–1424, DOI: 10.1021/acs.macromol.0c02493.
47 T. E. Gartner, III, M. A. Morris, C. K. Shelton, J. A. Dura and T. H. Epps, III, *Macromolecules*, 2018, **51**, 1917–1926, DOI: 10.1021/acs.macromol.7b02600.
48 A. A. Teran and N. P. Balsara, *J. Phys. Chem. B*, 2014, **118**, 4–17, DOI: 10.1021/jp408079z.
49 M. Safari, C. Ocando, Y. Liao, M. Drechsler, N. Volk, R. Schaller, M. Held, V. Abetz, H. Schmalz and A. J. Müller, *Polymer*, 2024, **298**, 126863, DOI: 10.1016/j.polymer.2024.126863.
50 R. Kato, S. Nakagawa, H. Marubayashi and S. Nojima, *Macromolecules*, 2016, **49**, 5955–5962, DOI: 10.1021/acs.macromol.6b00877.
51 Y.-L. Loo, R. A. Register and A. J. Ryan, *Macromolecules*, 2002, **35**, 2365–2374, DOI: 10.1021/ma011824j.
52 S. Z. D. Cheng, A. Q. Zhang, J. H. Chen and D. P. Heberer, *J. Polym. Sci., Part B:Polym. Phys.*, 1991, **29**, 287–297, DOI: 10.1002/polb.1991.090290304.
53 Y. S. Sun, T. M. Chung, Y. J. Li, R. M. Ho, B. T. Ko, U. S. Jeng and B. Lotz, *Macromolecules*, 2006, **39**, 5782–5788, DOI: 10.1021/ma0608121.
54 Y.-L. Loo, R. A. Register, A. J. Ryan and G. T. Dee, *Macromolecules*, 2001, **34**, 8968–8977, DOI: 10.1021/ma011521p.
55 C. T. Yu, Q. Xie, Y. Z. Bao, G. R. Shan and P. J. Pan, *Crystals*, 2017, **7**, 147, DOI: 10.3390/cryst7050147.

56 P. Huang, Y. Guo, R. P. Quirk, J. Ruan, B. Lotz, E. L. Thomas, B. S. Hsiao, C. A. Avila-Orta, I. Sics and S. Z. D. Cheng, *Polymer*, 2006, **47**, 5457–5466, DOI: **10.1016/j.polymer.2005.06.129**.

57 P. Huang, J. X. Zheng, S. Leng, R. M. Van Horn, K.-U. Jeong, Y. Guo, R. P. Quirk, S. Z. D. Cheng, B. Lotz, E. L. Thomas and B. S. Hsiao, *Macromolecules*, 2007, **40**, 526–534, DOI: **10.1021/ma061871h**.

58 W. Lee, H. L. Chen and T. L. Lin, *J. Polym. Sci., Part B:Polym. Phys.*, 2002, **40**, 519–529, DOI: **10.1002/polb.10121**.

59 A. J. Müller, R. V. Castillo and M. Hillmyer, *Macromol. Symp.*, 2006, **242**, 174–181, DOI: **10.1002/masy.200651025**.

60 P. A. Weimann, D. A. Hajduk, C. Chu, K. A. Chaffin, J. C. Brodil and F. S. Bates, *J. Polym. Sci., Part B:Polym. Phys.*, 1999, **37**, 2053–2068, DOI: **10.1002/(sici)1099-0488(19990815)37:16<2053::Aid-polb9>3.3.Co;2-c**.

61 M. Singh, O. Odusanya, G. M. Wilmes, H. B. Eitouni, E. D. Gomez, A. J. Patel, V. L. Chen, M. J. Park, P. Fragouli, H. Iatrou, N. Hadjichristidis, D. Cookson and N. P. Balsara, *Macromolecules*, 2007, **40**, 4578–4585, DOI: **10.1021/ma0629541**.

62 W.-S. Young and T. H. Epps, *Macromolecules*, 2012, **45**, 4689–4697, DOI: **10.1021/ma300362f**.

63 R. Yuan, A. A. Teran, I. Gurevitch, S. A. Mullin, N. S. Wanakule and N. P. Balsara, *Macromolecules*, 2013, **46**, 914–921, DOI: **10.1021/ma3024552**.

64 H. Xu and M. K. Mahanthappa, *Macromolecules*, 2021, **54**, 8798–8809, DOI: **10.1021/acs.macromol.1c01100**.